

APPROXIMATE MARGINALIZATION OF ABSORPTION AND SCATTERING IN FLUORESCENCE DIFFUSE OPTICAL TOMOGRAPHY

MEGHDOOT MOZUMDER AND TANJA TARVAINEN

Department of Applied Physics, University of Eastern Finland, P.O. Box 1627, 70211 Kuopio, Finland

SIMON ARRIDGE

Department of Computer Science, University College London, Gower Street, London WC1E 6BT, UK

JARI P. KAIPIO

Department of Mathematics, University of Auckland, Private Bag 92019, Auckland Mail Centre, Auckland 1142, New Zealand

COSIMO D' ANDREA

Center for Nanoscience and Technology, Italian Institute of Technology, Polytechnic University of Milan, 20133 Milan, Italy

VILLE KOLEHMAINEN

Department of Applied Physics, University of Eastern Finland, P.O. Box 1627, 70211 Kuopio, Finland

(Communicated by the associate editor name)

ABSTRACT. In fluorescence diffuse optical tomography (fDOT), the reconstruction of the fluorophore concentration inside the target body is usually carried out using a normalized Born approximation model where the measured fluorescent emission data is scaled by measured excitation data. One of the benefits of the model is that it can tolerate inaccuracy in the absorption and scattering distributions that are used in the construction of the forward model to some extent. In this paper, we employ the recently proposed Bayesian approximation error approach to fDOT for compensating for the modeling errors caused by the inaccurately known optical properties of the target in combination with the normalized Born approximation model. The approach is evaluated using a simulated test case with different amount of error in the optical properties. The results show that the Bayesian approximation error approach improves the tolerance of fDOT imaging against modeling errors caused by inaccurately known absorption and scattering of the target.

1. Introduction. Fluorescence diffuse optical tomography (fDOT) is an emerging imaging technique aiming at recovering the distribution of fluorophore marker inside diffusive target medium from measurements of fluorescent emission at the surface of the body [1, 2]. Typically, fluorescence agents bound to molecules or proteins are introduced to the bloodstream. The molecules then act as ligands as they attach themselves to the targeted receptor sites. The surface of the body is illuminated with light at the excitation wavelength of the fluorescence agent. The measurement system collects fluence from the body surface at the emission wavelength. The

2010 *Mathematics Subject Classification.* Primary: 74J25, 92C55; Secondary: 65R32.

Key words and phrases. Image reconstruction techniques, Tomography, Inverse problems, Bayesian methods, Fluorescence diffuse optical tomography.

inverse problem associated with fDOT is the estimation of spatially distributed fluorophore marker concentration in the body.

In small animal studies [3, 2, 4], fDOT has been used for monitoring tumors in brain [5, 6], breast [7, 8] and lungs [9]. fDOT has also been used to monitor brain strokes [10], localizing lymph nodes that get affected at the onset of cancer [11] and studying the effects of drugs on tumor [12]. In humans, fDOT has been used in imaging breast cancer [1, 13, 14, 15].

Computationally, the inverse problem in fDOT amounts to estimating the spatially distributed fluorophore concentration from the model

$$y = A(\mu_a, \mu'_s)h + e, \quad (1)$$

where $h \in \mathbb{R}^n$ is the vector of unknowns, representing a pixel or voxel or other parametrization of the fluorophore concentration, $y \in \mathbb{R}^m$ is the measurement vector, $e \in \mathbb{R}^m$ models the measurement noise and $A(\mu_a, \mu'_s)$ is matrix implementing the forward model (i.e., the light propagation model) corresponding to nominal absorption and scattering distributions μ_a and μ'_s . The estimation of h from the model (1) is an ill-posed inverse problem, that is sensitive with respect to measurement and modeling errors.

The fDOT inverse problem is most often carried out using the so-called normalized Born approximation model [16], where the measurement vector is the measured fluorescent emission data vector y_{obs}^f scaled by the measured excitation data y_{obs}^e as

$$y = \frac{y_{\text{obs}}^f}{y_{\text{obs}}^e}, \quad (2)$$

and forward matrix A is

$$A(\mu_a, \mu'_s) = \text{diag}\left(\frac{1}{y_{\text{calc}}^e}\right)\tilde{A}(\mu_a, \mu'_s) \quad (3)$$

where \tilde{A} is the forward matrix corresponding to the raw fluorescence measurement and y_{calc}^e is computed excitation data corresponding to the absorption and scattering distributions μ_a and μ'_s [16, 17]. The convenience of the Born normalization comes from the fact that it does not require a reference excitation measurement from homogeneous reference media. The normalization also effectively calibrates the problem with respect to source strength and individual gains and coupling coefficients of individual source detector pairs [16, 4]. From the practical point of view, a further significant feature of the Born normalized model is that it can tolerate inaccurately known target absorption and scattering distributions (μ_a, μ'_s) to some extent.

The absorption and scattering distributions (μ_a, μ'_s) are often interpreted as known (nuisance) parameters in the fDOT problem. However, in practical experiments, the actual values of these parameters are usually not known accurately, and therefore one is bound to use approximate measurement model

$$y \approx A(\mu_{a,*}, \mu'_{s,*})h + e, \quad (4)$$

where $\mu_{a,*}$ and $\mu'_{s,*}$ are our estimates for the absorption and scattering of the body. Obviously, the use of incorrect realizations $(\mu_{a,*}, \mu'_{s,*})$ in the measurement model induces unknown modeling error

$$[A(\mu_a, \mu'_s) - A(\mu_{a,*}, \mu'_{s,*})]h$$

in the model, and since the inverse problem is ill-posed, this error may cause large artifacts to the reconstructed fluorophore image.

In this paper, we propose the reduction of the reconstruction errors caused by inaccurately known absorption and scattering of the body by the Bayesian approximation error approach [18, 19]. We consider the approach using the Born normalized model (1-3), so that the starting point would be the model that has the best available tolerance for the inaccurately known absorption and scattering. The key idea in the Bayesian approximation error model is to represent not just the measurement error, but also computational model inaccuracy as a random variable. Hence, instead of the approximate measurement model (4), we write an *accurate* measurement model,

$$y = A(\mu_{a,*}, \mu'_{s,*})h + \underbrace{[A(\mu_a, \mu'_s)h - A(\mu_{a,*}, \mu'_{s,*})h]}_{\varepsilon(\mu_a, \mu'_s, h)} + e \quad (5)$$

$$= A(\mu_{a,*}, \mu'_{s,*})h + \nu \quad (6)$$

where the term $\varepsilon = [A(\mu_a, \mu'_s) - A(\mu_{a,*}, \mu'_{s,*})]h$ represents the approximation error and $\nu = \varepsilon + e$ the total noise. Obviously, the realization of ε is unknown since it depends on the unknown h and the unknown nuisance parameters (μ_a, μ'_s) . However, in the Bayesian inversion paradigm, we can compute an estimate for the statistics of the approximation error ε over the prior probability distributions of the unknowns and the nuisance parameters μ_a and μ'_s . The approximation error statistics are then used in the inverse problem to compensate for the inaccurately known μ_a and μ'_s .

The Bayesian approximation error approach was originally applied for discretization error in several different applications in Ref. [18]. For this reason, the term “approximation error” is commonly used also where “modeling error” might be a more appropriate term. The approach was verified with real EIT data in Ref. [20], where the approach was employed for the compensation of discretization errors and the errors caused by inaccurately known height of the air-liquid surface in an industrial mixing tank. The application of the Bayesian approximation error approach for the discretization errors and the truncation of the computational domain was studied in Ref. [21], and for the linearization error in Ref. [22]. In Ref. [23] the approach was evaluated for the compensation of errors caused by coarse discretization, domain truncation and unknown contact impedances with real EIT data. In addition to EIT, the Bayesian approximation error approach has also been applied to other inverse problems and other types of (modeling) errors: Model reduction, domain truncation and unknown anisotropy structures in optical diffusion tomography were treated in Refs. [24], [25], [26] and [27]. Missing boundary data in the case of image processing was considered in Ref. [28]. In Ref. [29], again related to optical tomography, an approximative physical model (diffusion model instead of the radiative transfer model) was used for the forward problem. In Ref. [30], an unknown nuisance distributed parameter (scattering coefficient) was treated with the Bayesian approximation error approach. The compensation of errors caused by unknown optode coupling coefficients and locations was considered in Ref. [31]. The compensation of errors caused by unknown domain shape and discretization error was considered in Ref. [32]. The extension and application of the modeling error approach to time-dependent inverse problems was considered in Refs. [33], [34] and [35].

In this work, we evaluate the Bayesian approximation error approach with simulated two dimensional (2D) and three dimensional (3D) examples. In the 2D example, we use different levels of severity of error in the nominal absorption and scattering distributions and show that the approach improves the tolerance of the

fDOT problem against inaccurately known absorption and scattering of the body over the conventional reconstruction approach. In the 3D example, we test the approach using simulated data using the Digamous atlas geometry [36, 37].

The remainder of the paper is organized as follows. In Section 2, the Bayesian approximation error model for the compensation of modeling errors due to unknown absorption and scattering in fDOT is presented. In Section 3, we review the light transport model which we use for the forward model. The details of data simulation, meshing, constructing the prior models and estimation of the approximation error statistics are described in Section 4. The simulation results are presented in Section 5. Finally, the conclusions are given in Section 6.

2. Bayesian approximation error approach.

2.1. Statistical inversion in general. In the Bayesian approach to inverse problems, the principle is that all unknowns and measured quantities are considered as random variables and the uncertainty of their values are encoded into their probability distribution models [18, 38]. The complete model of the inverse problem is the posterior density model, that is, the information and uncertainties in the unknown or interesting variables given the measurements, given by the Bayes' theorem

$$\pi(h, \mu_a, \mu'_s, e|y) = \frac{\pi(y|h, \mu_a, \mu'_s, e)\pi(h, \mu_a, \mu'_s, e)}{\pi(y)}, \quad (7)$$

where $\pi(y|h, \mu_a, \mu'_s, e)$ is the likelihood density modeling the probability of different measurement realizations when the realizations of h , μ_a , μ'_s and e are given. The density $\pi(h, \mu_a, \mu'_s, e)$ is the prior model and it models our information on the unknown parameters before the actual measurements. The posterior (7) is practically always marginalized with respect to the unknown but uninteresting measurement related errors e as

$$\pi(h, \mu_a, \mu'_s|y) = \int \pi(h, \mu_a, \mu'_s, e|y)de, \quad (8)$$

for details in the case of the additive error model $y = A(h) + e$, see Refs. [30] and [39], for other types of errors see Ref. [18]. The posterior density $\pi(h, \mu_a, \mu'_s|y)$ is a probability density in a very high-dimensional space. Thus, in order to get practical estimates for the unknowns and visualize the solution, one needs to compute point estimate(s) from the posterior density, the most common choice in high dimensional cases being the *maximum a posteriori* (MAP) estimate. In principle, one could attempt to compute the MAP estimate for all the unknown model parameters

$$(h, \mu_a, \mu'_s)_{\text{MAP}} = \arg \max_{h, \mu_a, \mu'_s} \pi(h, \mu_a, \mu'_s|y). \quad (9)$$

See Refs. [40], [41] and [42] for simultaneous reconstruction of fluorescent and optical parameters. Also, in Ref. [43] a method to determine a modified optical parameter (related to μ_a, μ'_s) from measured excitation data and include it as apriori anatomical information into fDOT imaging is presented. Alternatively, one could treat the uncertainty in the values of nuisance parameters (μ_a, μ'_s) by marginalizing the posterior density as

$$\pi(h|y) = \int \int \pi(h, \mu_a, \mu'_s|y)d\mu_a d\mu'_s \quad (10)$$

and then compute estimate for the primary unknowns from the posterior $\pi(h|y)$. However, the solution of (10) would require Markov chain Monte Carlo integrations that would be computationally infeasible for practical purposes.

The key idea in the Bayesian approximation error approach is to find an approximation $\tilde{\pi}(h|y)$ for the posterior (10) such that the marginalization over the uncertainty in the values of (μ_a, μ'_s) is carried out *approximately* and in a computationally feasible way.

Before presenting the Bayesian approximation error approach for treating the uncertainty in the optical parameters (μ_a, μ'_s) , we first review the standard fDOT reconstruction approach where $(\mu_a, \mu'_s) = (\mu_{a,*}, \mu'_{s,*})$ are treated as known and fixed variables.

2.2. Conventional error model. In most of fDOT reconstruction schemes, the optical parameters (μ_a, μ'_s) are treated as known (fixed) nuisance parameters with values $\mu_a = \mu_{a,*}$ and $\mu'_s = \mu'_{s,*}$. Within the Bayesian setup, this is equivalent to considering (μ_a, μ'_s) as fixed conditioning parameters, leading to posterior density model

$$\pi(h, e|y, \mu_a = \mu_{a,*}, \mu'_s = \mu'_{s,*}) = \frac{\pi(y|h, \mu_a = \mu_{a,*}, \mu'_s = \mu'_{s,*}, e)\pi(h)\pi(e)}{\pi(y)}. \quad (11)$$

However, in cases that the values $(\mu_{a,*}, \mu'_{s,*})$ are incorrect, the model (11) can be grossly misleading.

Given the observation model (4) with fixed realizations $(\mu_a, \mu'_s) = (\mu_{a,*}, \mu'_{s,*})$, and modeling the measurement noise as normal $e \sim \mathcal{N}(e_*, \Gamma_e)$, where $e_* \in \mathbb{R}^m$ is the measurement noise mean and $\Gamma_e \in \mathbb{R}^{m \times m}$ is the measurement noise covariance and marginalizing (11) over the unknown measurement errors e as

$$\pi(h|y, \mu_{a,*}, \mu'_{s,*}) = \int \pi(h, e|y, \mu_{a,*}, \mu'_{s,*})de$$

the posterior density becomes [30, 39]

$$\pi(h|y, \mu_{a,*}, \mu'_{s,*}) \propto \exp \left\{ -\frac{1}{2} \|y - A(\mu_{a,*}, \mu'_{s,*})h - e_*\|_{\Gamma_e^{-1}}^2 \right\} \pi(h) \quad (12)$$

In addition, if the random measurement noise has zero mean ($e_* = 0$), the MAP estimate corresponding to the posterior (12) is obtained as

$$\begin{aligned} h_{\text{cem}} &= \arg \max_h \pi(h|y, \mu_a = \mu_{a,*}, \mu'_s = \mu'_{s,*}) \\ &= \arg \min_h \{ \|y - A(\mu_{a,*}, \mu'_{s,*})h\|_{\Gamma_e^{-1}}^2 - 2 \log \pi(h) \}, \end{aligned} \quad (13)$$

where the Cholesky factor $L_e^T L_e = \Gamma_e^{-1}$. We refer to the solution of (13) as the MAP estimate with the conventional error model (CEM) approach.

2.3. Bayesian approximation error model. In the Bayesian approximation error approach, we write the measurement model as

$$y = A(\mu_{a,*}, \mu'_{s,*})h + \underbrace{[A(\mu_a, \mu'_s)h - A(\mu_{a,*}, \mu'_{s,*})h]}_{\varepsilon(\mu_a, \mu'_s, h)} + e \quad (14)$$

$$= A(\mu_{a,*}, \mu'_{s,*})h + \nu \quad (15)$$

Note that the model (15) is exact, see equation (1). Here the term $\varepsilon = [A(\mu_a, \mu'_s) - A(\mu_{a,*}, \mu'_{s,*})]h$ represents the approximation error and $\nu = \varepsilon + e$ the total error. Obviously, the realization of ε is unknown since it depends on the unknowns h and the unknown nuisance parameters (μ_a, μ'_s) . However, in the Bayesian inversion

paradigm we can compute an estimate of the statistics of ε using the prior probability distributions of the unknowns and the nuisance parameters and approximately marginalize over ε .

To include the uncertainty in the noise process ε into our computational posterior model, the core step in the Bayesian approximation error approach is approximate pre-marginalization of the joint distribution of the parameters $(y, h, e, \varepsilon, \mu_a, \mu'_s)$ over the nuisance parameters $(e, \varepsilon, \mu_a, \mu'_s)$. Following the approach in Refs. [30] and [39] and making a Gaussian approximation for the joint density $\pi(h, \varepsilon)$, we obtain the approximate likelihood model

$$\tilde{\pi}(y|h) \propto \exp \left\{ -\frac{1}{2} \|y - A(\mu_{a,*}, \mu'_{s,*})h - \nu_{*|h}\|_{\Gamma_{\nu|h}^{-1}}^2 \right\} \quad (16)$$

where

$$\nu_{*|h} = e_* + \varepsilon_* + \Gamma_{\varepsilon,h} \Gamma_h^{-1} (h - h_*) \quad (17)$$

$$\Gamma_{\nu|h} = \Gamma_e + \Gamma_\varepsilon - \Gamma_{\varepsilon,h} \Gamma_h^{-1} \Gamma_{h,\varepsilon} \quad (18)$$

For the posterior model, we write an approximation $\tilde{\pi}(h|y) \propto \tilde{\pi}(y|h)\pi(h)$, leading to MAP estimation problem

$$h_{\text{aem}} = \arg \min_h \{ \|y - A(\mu_{a,*}, \mu'_{s,*})h - \nu_{*|h}\|_{\Gamma_{\nu|h}^{-1}}^2 - 2 \log \pi(h) \}. \quad (19)$$

We refer to the estimate (19) as the MAP with the Bayesian approximation error model (MAP-AEM).

In the following, we employ the *enhanced error model* [18, 19], where we approximate the error ε and the unknown h as mutually uncorrelated, implying that the mean and covariance in equations (17)-(18) become

$$\nu_{*|h} \approx e_* + \varepsilon_*, \quad \Gamma_{\nu|h} \approx \Gamma_e + \Gamma_\varepsilon.$$

In this work, the mean ε_* and covariance Γ_ε were computed by sampling based Monte Carlo integration (see Section 4.3).

2.4. Estimates to be computed. To evaluate the Bayesian approximation error approach, we compute the following estimates

(MAP-REF): The unknown h_{cem} using correct fixed optical coefficients (μ_a, μ'_s) :

$$h_{\text{ref}} = \arg \min_h \{ \|y - A(\mu_a, \mu'_s)h\|_{\Gamma_e^{-1}}^2 - 2 \log \pi(h) \}. \quad (20)$$

In other words, in MAP-REF (μ_a, μ'_s) are known exactly. Therefore, this estimate serves as reference of conventional reconstruction when (μ_a, μ'_s) are known.

(MAP-CEM): The unknown h_{cem} using incorrect fixed optical coefficients $(\mu_{a,*}, \mu'_{s,*})$ (Eq. 13). This estimate serves as a conventional reconstruction when nominal (μ_a, μ'_s) are incorrect.

(MAP-AEM): The unknown h_{aem} using the same fixed incorrect coefficients $(\mu_{a,*}, \mu'_{s,*})$ (Eq. 19). This estimate serves as a Bayesian approximation error model reconstruction when nominal (μ_a, μ'_s) are incorrect.

The values $(\mu_{a,*}, \mu'_{s,*})$ in the computations correspond to the expectations of the (proper Gaussian smoothness) prior models $\pi(\mu_a)$ and $\pi(\mu'_s)$, respectively. The prior means were homogeneous distributions with $\mu_{a,*}(r) \equiv 0.01\text{mm}^{-1}$ and $\mu'_{s,*}(r) \equiv 1\text{mm}^{-1}$.

3. Forward model. Let $\Omega \subset \mathbb{R}^n$, $n = 2, 3$, denote the object domain. In a diffusive medium like soft tissue, the commonly used light transport model for excitation and fluorescence light is the diffusion approximation (DA) to the radiative transport equation (RTE) [44]. In this paper the DC (zero-frequency) domain version of the diffusion approximation is used

$$(-\nabla \cdot \kappa(r)\nabla + \mu_a(r))\Phi^e(r) = 0, \quad r \in \Omega, \quad (21)$$

$$\Phi^e(r) + \frac{1}{2\zeta}\kappa(r)\alpha\frac{\partial\Phi^e(r)}{\partial\vartheta} = \begin{cases} \frac{q(r)}{\zeta} & r \in r_s \\ 0 & r \in \partial\Omega \setminus r_s \end{cases}, \quad (22)$$

$$(-\nabla \cdot \kappa(r)\nabla + \mu_a(r))\Phi^f(r) = h(r)\Phi^e(r), \quad r \in \Omega, \quad (23)$$

$$\Phi^f(r) + \frac{1}{2\zeta}\kappa(r)\alpha\frac{\partial\Phi^f(r)}{\partial\vartheta} = 0, \quad r \in \partial\Omega, \quad (24)$$

where $\Phi^e(r) := \Phi^e$ is the excitation photon density, $\Phi^f(r) := \Phi^f$ is the fluorescence emission photon density, $\mu_a(r) := \mu_a$ is the absorption coefficient, $\kappa(r) := \kappa$ is the diffusion coefficient. The diffusion coefficient κ is given by $\kappa(r) = 1/(n(\mu_a(r) + \mu'_s(r)))$, where $\mu'_s(r) := \mu'_s$ is the reduced scattering coefficient. For simplicity the spectral dependency of the optical properties (μ_a, μ'_s) is omitted and they are modelled the same at the excitation and emission wavelengths. The parameter $h(r) := h$ is the fluorophore concentration. The parameter $q(r)$ is the strength of the light source at location $r_s \subset \partial\Omega$. The parameter ζ is a dimension dependent constant ($\zeta = 1/\pi$ when $\Omega \subset \mathbb{R}^2$, $\zeta = 1/2$ when $\Omega \subset \mathbb{R}^3$), α is a parameter governing the internal reflection at the boundary $\partial\Omega$ and ϑ is the outward normal to the boundary at point r . The measurable excitation data and fluorescence emission data (Eq. 2) are given by

$$y^e(r) = -\kappa\frac{\partial\Phi^e(r)}{\partial\vartheta} = \frac{2\gamma}{\alpha}\Phi^e(r), \quad r \in r_d, \quad (25)$$

$$y^f(r) = -\kappa\frac{\partial\Phi^f(r)}{\partial\vartheta} = \frac{2\gamma}{\alpha}\Phi^f(r), \quad r \in r_d, \quad (26)$$

where $r_d \subset \partial\Omega$ are the detector locations.

For the inverse problem, the mapping $A(\mu_a, \mu'_s)h$ (Eq. (1)) is given by [16, 4, 17]

$$A(\mu_a, \mu'_s)h = \frac{\int_{\Omega} \Phi^e(r_s, r)\Psi^e(r_d, r)h(r)dr}{\int_{\Omega} \Phi^e(r_s, r)dr}, \quad (27)$$

where $\Phi^e(r_s, r)$ is the computed excitation photon density due to source $q(r)$. $\Psi^e(r_d, r)$ is the computed adjoint solution (photon density due to sources placed at detector locations r_d).

The numerical approximation of the forward model used here is based on a finite element method (FEM) solution of Eq. (21-26).

4. Computation details.

4.1. Simulation of the measurement data.

4.1.1. *2D simulations.* In the 2D numerical studies, the domain $\Omega \subset \mathbb{R}^2$ was a disk with radius $r = 25\text{mm}$. The measurement setup consisted of 16 sources and 16 detectors. The source and detector optodes were modeled as 1mm wide surface patches located at equi-spaced angular intervals on the boundary $\partial\Omega$. With this setup, the vector of fDOT measurements (2) was $y \in \mathbb{R}^{256}$. Five targets with different optical properties of absorption and scattering were used in the simulations (see Fig. 2, column 1, 2). The fluorophore concentrations of these targets is shown in column 1, Fig. 3. For the simulation of the measurement data, a mesh with 33806 nodes and 67098 triangular elements was used. In the inverse problem, a FEM mesh with 26075 nodes and 51636 elements was used.

4.1.2. *3D simulations.* In the 3D simulations, the domain $\Omega \subset \mathbb{R}^3$ was a mouse atlas ‘‘Digimouse’’ [36, 37]. The measurement setup consisted of 32 sources and 32 detectors (see Fig. 4, bottom right). The source and detector optodes were modeled as 1mm wide surface patches placed on the top-surface of the boundary $\partial\Omega$. With this setup, the vector of fDOT measurements (2) was $y \in \mathbb{R}^{512}$. The optical properties of the target are shown in column 1, Fig. 4. The fluorophore concentrations of the target is shown in column 2, Fig. 4. For generating the measurement data and for the inverse problem we used the same mesh obtained from the Digimouse website [37] which had 58244 nodes and 306773 elements.

The simulated measurement data was generated using the FEM approximation of Eq (21)-(26). Random measurement noise, drawn from a zero-mean Gaussian distribution was added separately to the simulated measurement excitation and fluorescence emission data as,

$$\frac{y_{\text{obs}}^f}{y_{\text{obs}}^e} = \frac{y_{\text{calc}}^f + e^f}{y_{\text{calc}}^e + e^e} \quad (28)$$

$$= y_{\text{calc}} + e. \quad (29)$$

Here $e^f \sim \mathcal{N}(0, \text{diag}(\sigma_{e^f,1}, \dots, \sigma_{e^f,m})) \in \mathbb{R}^m$ is the noise added to the fluorescence emission data, $e^e \sim \mathcal{N}(0, \text{diag}(\sigma_{e^e,1}, \dots, \sigma_{e^e,m})) \in \mathbb{R}^m$ is the noise added to the excitation data. The standard deviations $\{\sigma_{e^e,1}, \dots, \sigma_{e^e,m}\}$ and $\{\sigma_{e^f,1}, \dots, \sigma_{e^f,m}\}$ were specified as 1% of the simulated noise free measurement excitation and fluorescence emission data, y_{calc}^e and y_{calc}^f respectively.

In order to estimate the noise statistics for the inverse problem, a Gaussian approximation for the measurement noise e , $\pi(e) = \mathcal{N}(0, \Gamma_e)$ was constructed. The covariance Γ_e was approximated by a diagonal where the diagonal elements (i.e., standard deviations of the measurements) were estimated as sample averages from 100 noisy realizations of the Born ratio (Eq. (28)). In a practical setup, similar estimation of Γ_e can be carried out by repeated measurements from a phantom target.

4.2. **Prior models.** For drawing the samples of optical coefficients x , where

$$x = (\mu_a, \mu'_s, h)^T,$$

for the estimation of the approximation error statistics, we used a Gaussian (Markov random field) [45] prior model along with non-negativity constraint [46],

$$\pi(x) = \pi_G(x)\pi_+(x). \quad (30)$$

Here $\pi_G(x)$ is a Gaussian smoothness prior model and $\pi_+(x)$ is the non-negativity constraint. Section 4.2.1 describes the implementation of the Gaussian smoothness prior model, Section 4.2.2 describes the implementation of non-negativity constraint.

4.2.1. *Proper Gaussian smoothness prior.* As we need to draw samples of the unknown x for the estimation of approximation errors, we need a proper (integrable) prior distribution for the unknowns. In this study we used a proper Gaussian smoothness prior $\pi_G(x)$ for the unknowns. In this model, the absorption, scattering and fluorophore concentration images μ_a , μ'_s and h were modeled as mutually independent Gaussian random fields with a joint prior model

$$\pi_G(x) \propto \exp\left\{-\frac{1}{2}\|L_x(x - x_*)\|^2\right\}, \quad L_x^T L_x = \Gamma_x^{-1} \quad (31)$$

where

$$x_* = \begin{pmatrix} \mu_{a,*} \\ \mu'_{s,*} \\ h_* \end{pmatrix}, \quad \Gamma_x = \begin{pmatrix} \Gamma_{\mu_a} & 0 & 0 \\ 0 & \Gamma_{\mu'_s} & 0 \\ 0 & 0 & \Gamma_h \end{pmatrix}.$$

In the construction of the mean vectors $\mu_{a,*}$, $\mu'_{s,*}$, h_* and covariances Γ_{μ_a} , $\Gamma_{\mu'_s}$ and Γ_h , the random field, say f (i.e., either μ_a , μ'_s or h), is considered in the form

$$f = f_{\text{in}} + f_{\text{bg}}$$

where f_{in} is a spatially inhomogeneous parameter with zero mean,

$$f_{\text{in}} \sim \mathcal{N}(0, \Gamma_{\text{in},f})$$

and f_{bg} is a spatially constant (background) parameter with non-zero mean. For the latter, we can write $f_{\text{bg}} = q\mathbb{I}$, where $\mathbb{I} \in \mathbb{R}^n$ is a vector of ones and q is a scalar random variable with distribution $q \sim \mathcal{N}(c, \sigma_{\text{bg},f}^2)$. In the construction of $\Gamma_{\text{in},f}$, the approximate correlation length can be adjusted to match the size of the expected inhomogeneities and the marginal variances of f_k 's are tuned based on the expected contrast of the inclusions. We model the distributions f_{in} and f_{bg} as mutually independent, that is, the background is mutually independent with the inhomogeneities. Thus, we have

$$f_* = c\mathbb{I}, \quad \Gamma_f = \Gamma_{\text{in},f} + \sigma_{\text{bg},f}^2 \mathbb{I}\mathbb{I}^T$$

See [18, 24, 30] for further details, and see [47] for an alternative construction of a proper smoothness prior.

The parameters in the prior model $\pi(x)$ were selected as follows. The mean for background absorption, scattering and fluorophore concentration were set as $\mu_{a,*} = 0.01\text{mm}^{-1}$, $\mu'_{s,*} = 1\text{mm}^{-1}$ and $h_* = 0\text{mm}^{-1}$. The standard deviations σ_{bg,μ_a} and $\sigma_{\text{bg},\mu'_s}$ of the background values were chosen such that 2 s.t.d. limits equaled 25% of the mean values $\mu_{a,*}$ and $\mu'_{s,*}$ and the standard deviation $\sigma_{\text{bg},h}$ of the background value for h was chosen as 0.25mm^{-1} . In the construction of $\Gamma_{\text{in},f}$, the correlation length for μ_a , μ'_s and h in the prior was set as 16mm. The marginal standard deviations were set to equal values in each pixel and σ_{in,μ_a} and $\sigma_{\text{in},\mu'_s}$ were chosen such that 2 s.t.d. limits equaled 50% of the mean values $\mu_{a,*}$ and $\mu'_{s,*}$. $\sigma_{\text{in},h}$ was chosen as 1mm^{-1} . Thus, the overall marginal variances (i.e., diagonal elements of Γ_{μ_a} , $\Gamma_{\mu'_s}$ and Γ_h) were $2\sigma_{\mu_a} = 0.0056\text{mm}^{-1}$, $2\sigma_{\mu'_s} = 0.56\text{mm}^{-1}$ and $2\sigma_h = 1\text{mm}^{-1}$. This gives overall 2 s.t.d. intervals $\mu_a \in [0.0044, 0.0156]\text{mm}^{-1}$, $\mu'_s \in [0.44, 1.56]\text{mm}^{-1}$ and $h \in [-1, 1]$ i.e., the values of absorption, scattering and fluorophore concentration are expected to lie within these intervals with *prior*

probability of 95%. The same prior parameters (correlation length, means and standard deviations) are used in 2D and 3D priors.

4.2.2. *Non-negativity constraint.* In addition to the Gaussian smoothness prior, a non-negativity constraint was applied while drawing samples for the computation of approximation error statistics. A tolerance value for the values of x was chosen and the values of x drawn from prior $\pi_G(x)$ that were less than the tolerance value, were set equal to the tolerance value as,

$$x = \max(x, \text{tol}). \quad (32)$$

Here “tol” is the tolerance value, $\text{tol} = 10e^{-6}$ was used in this study.

Two random draws of $x = (\mu_a, \mu'_s, h)^T$ from $\pi(x)$ in the 2D simulation domain are shown in Figure 1.

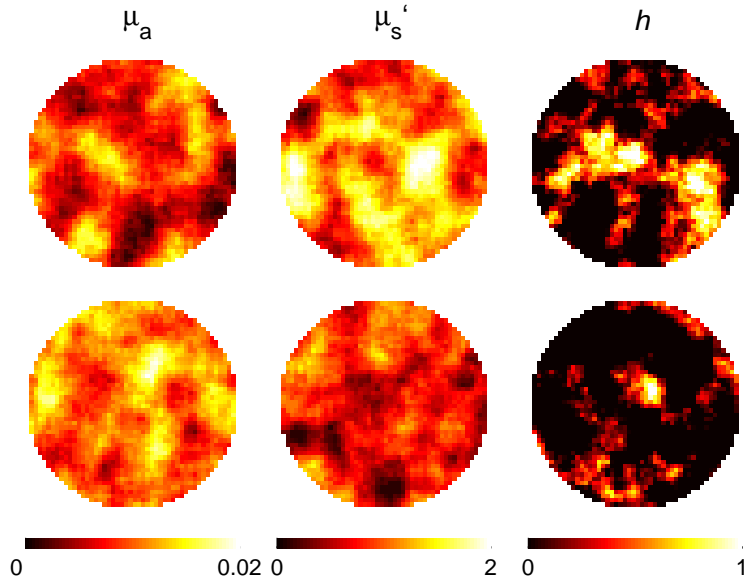


FIGURE 1. Two draws (top and bottom row) of μ_a , μ'_s and h from $\pi(x)$ in the 2D simulation domain. From left: first column is μ_a , second column is μ'_s and third column is h .

The non-negativity prior during the computation of the MAP estimates (20), (13), (19) is taken into account by applying an exterior point search method [46]. In this method, the non-negativity problem is approximated by a sequence of unconstrained problems

$$h_{\text{MAP}} = \arg \min_h \{-\log(\pi(h|y)) - \log(\pi(h))\}, \quad (33)$$

$$= \arg \min_h \{-2\log(\pi(h|y)) + \|L_h(h - h_*)\|^2 + E^j(h)\} \quad (34)$$

where $\pi(h|y)$ is the likelihood and $\pi(h)$ is the prior probability distribution. $E^j(h)$ is a penalty functional that is used to penalize the negative components of the solution h , the super index j is used to denote the j^{th} problem in the sequence. The mean $h_* \in \mathbb{R}^n$ and Cholesky factor $L_h^T L_h = \Gamma_h^{-1} \in \mathbb{R}^{n \times n}$ is obtained from the

Gaussian smoothness prior model $\pi_G(x)$. In this study we employ a functional of the form

$$E^j(h) = \sum_{k=1}^n \gamma^j \phi(h_k) \quad (35)$$

where

$$\phi(h_k) = \begin{cases} (h_k)^2, & h_k < 0 \\ 0, & \text{otherwise,} \end{cases} \quad (36)$$

and $\gamma^j, j = 1, 2, \dots, M$ is a sequence of increasing positive penalty parameters. The exterior point methods guarantee the non-negativity of the solution only in the asymptotic limit $j \rightarrow \infty$. In this paper, we used $\{\gamma^1 = 1, \gamma^2 = 10, \gamma^3 = 100\}$ as the sequence of exterior point parameters. The incorporation of the non-negativity constraint to the MAP estimates (20), (13), (19), leads to non-linear minimization problems, which were solved by a Gauss-Newton algorithm with an explicit line search algorithm [48].

4.3. Estimation of approximation error statistics. For the computation of the error statistics, first the samples of absorption, scattering and fluorophore concentrations

$$S = \{x^{(\ell)}, l = 1, \dots, N_s\} \quad (37)$$

were drawn. Two of the samples $x^{(\ell)}$ are shown in Figure 1. The samples were then used for the computation of the accurate forward solutions $A(\mu_a^{(\ell)}, \mu_s'^{(\ell)})h^{(\ell)}$ and approximate forward solutions $A(\mu_{a,*}, \mu_{s,*}')h^{(\ell)}$, and the samples of the approximation error

$$\varepsilon^{(\ell)} = [A(\mu_a^{(\ell)}, \mu_s'^{(\ell)}) - A(\mu_{a,*}, \mu_{s,*}')h^{(\ell)}],$$

were computed. Then the mean ε_* and covariance Γ_ε were estimated using the samples $\{\varepsilon^{(\ell)}\}$ as

$$\varepsilon_* = \frac{1}{N_s} \sum_{\ell=1}^{N_s} \varepsilon^{(\ell)} \quad (38)$$

$$\Gamma_\varepsilon = \frac{1}{N_s - 1} \sum_{\ell=1}^{N_s} (\varepsilon^{(\ell)} - \varepsilon_*)(\varepsilon^{(\ell)} - \varepsilon_*)^T. \quad (39)$$

5. Results.

5.1. 2D simulations. The true absorption and scattering parameters (μ_a, μ'_s) used in the simulations are shown in Figure 2, column 1 (absorption) and column 2 (scattering). The nominal values $(\mu_{a,*}, \mu_{s,*}')$ that are used in the estimates h_{cem} and h_{aem} are shown in Figure 2, column 3 (absorption), column 4 (scattering). The true target fluorophore distribution h is shown in first column in Figure 3. The MAP estimates with the measurement data from the target domains in columns 1 and 2 in Figure 2 are shown in Figure 3, column 2-4, in matching order of rows. The estimates are:

(MAP-REF): The MAP-ref estimates using correct fixed (μ_a, μ'_s)

$$h_{\text{ref}} = \arg \min_h \{ \|y - A(\mu_a, \mu'_s)h\|_{\Gamma_e^{-1}}^2 + \|L_h(h - h_*)\|^2 + E^j(h) \}, \quad (40)$$

are shown in column 2, Figure 3. This corresponds to the reference estimate of conventional reconstruction when (μ_a, μ'_s) are known exactly.

(MAP-CEM): The MAP-CEM estimates with fixed optical coefficients $(\mu_{a,*}, \mu'_{s,*})$

$$h_{\text{cem}} = \arg \min_h \{ \|y - A(\mu_{a,*}, \mu'_{s,*})h\|_{\Gamma_e^{-1}}^2 + \|L_h(h - h_*)\|^2 + E^j(h) \}, \quad (41)$$

are shown in column 3, Figure 3. This corresponds to estimate with conventional reconstruction when the nominal values of (μ_a, μ'_s) are incorrect.

(MAP-AEM): The MAP-AEM estimates with the same fixed optical coefficients $(\mu_{a,*}, \mu'_{s,*})$

$$h_{\text{aem}} = \arg \min_h \{ \|y - A(\mu_{a,*}, \mu'_{s,*})h - \nu_{*|h}\|_{\Gamma_{\nu|h}^{-1}}^2 + \|L_h(h - h_*)\|^2 + E^j(h) \}, \quad (42)$$

are shown in column 4, Figure 3. This corresponds to estimate with Bayesian approximation error model when the nominal values of (μ_a, μ'_s) are incorrect.

The relative error in the MAP estimates (40), (41), (42),

$$\text{Error} = \frac{\|h - h_{\text{true}}\|^2}{\|h_{\text{true}}\|^2} \times 100\%, \quad (43)$$

where h is the estimated fluorophore distribution and h_{true} is the true fluorophore distribution are shown in Table 1.

TABLE 1. Relative error (%) in MAP estimates (40), (41), (42) for each 2D simulation test cases (test cases are numbered from top to bottom in Fig 1 and 2).

Case	h_{ref}	h_{cem}	h_{aem}
1	42	42	59
2	38	64	61
3	44	100	66
4	42	117	62
5	43	116	66

5.2. 3D simulations. The true absorption and scattering parameters (μ_a, μ'_s) from horizontal and vertical slices of target mouse model used in the simulations are shown in Figure 4, column 1: top (absorption) and bottom (scattering). The true target fluorophore distribution h is shown in second column in Figure 4. The nominal values $(\mu_{a,*}, \mu'_{s,*})$ that are used in the estimates h_{cem} and h_{aem} are homogeneous distributions with $\mu_{a,*}(r) \equiv 0.01\text{mm}^{-1}$ and $\mu'_{s,*}(r) \equiv 1\text{mm}^{-1}$. The MAP estimates are:

(MAP-REF): shown in column 3, Figure 4. This corresponds to the reference estimate of conventional reconstruction when (μ_a, μ'_s) are known exactly.

(MAP-CEM): shown in column 4, Figure 4. This corresponds to estimate with conventional reconstruction when the nominal values of (μ_a, μ'_s) are incorrect.

(MAP-AEM): shown in column 5, Figure 4. This corresponds to estimate with Bayesian approximation error model when the nominal values of (μ_a, μ'_s) are incorrect.

The results show that the Bayesian approximation error model efficiently compensates for the modeling errors caused by inaccurately known (μ_a, μ'_s) of the body and produce estimates that are qualitatively similar to the conventional estimates

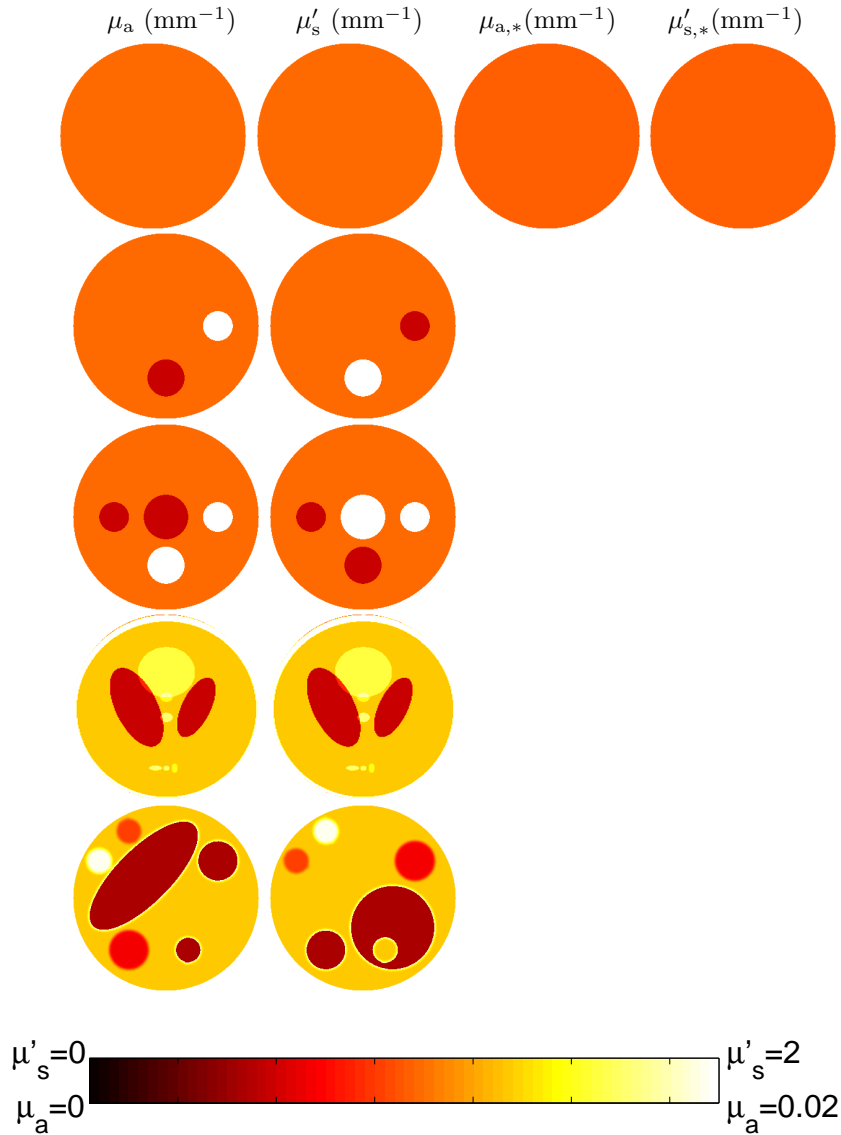


FIGURE 2. First and second columns show μ_a (left) and μ'_s (right) of the body Ω in test cases 1-5 (top to bottom). Third and fourth columns show the (incorrect) absorption and scattering $\mu_{a,*}$ and $\mu'_{s,*}$ that are used in the computation of the estimates MAP-CEM and MAP-AEM.

with exactly known μ_a and μ'_s . The inclusions in the fluorescent contrast are well localized with the Bayesian approximation error model and the estimates are relatively free of the artifacts that are present in the estimates h_{cem} with the conventional error model using the same incorrect values of $(\mu_{a,*}, \mu'_{s,*})$, see rows 2-5 in Figure 3 and columns 3-5 in Figure 4.

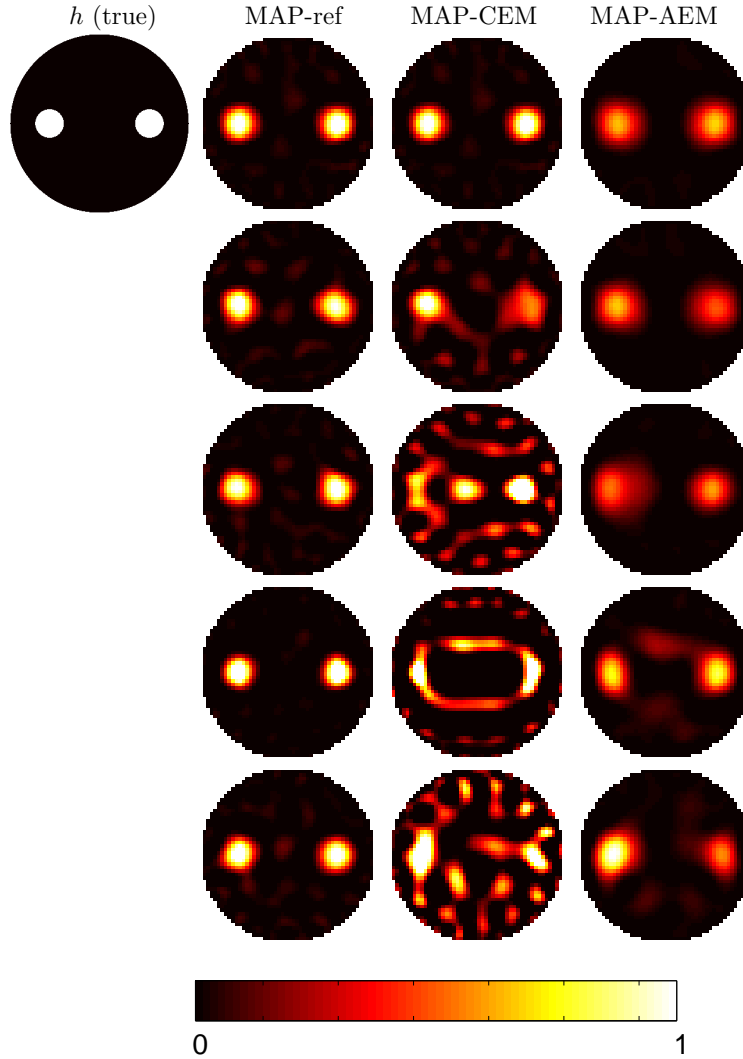


FIGURE 3. First column: fluorophore distribution h of the body Ω in test cases 1-5 (top to bottom). The second column shows the MAP-ref estimate using the correct absorption and scattering (forward matrix $A(\mu_a, \mu'_s)$). The absorption and scattering images μ_a and μ'_s are shown in columns 1 and 2 in Figure 2 (rows in respective order). Third column shows the the MAP-CEM estimate using the incorrect absorption and scattering values (forward matrix $A(\mu_{a,*}, \mu'_{s,*})$). The $\mu_{a,*}$ and $\mu'_{s,*}$ are shown in third and fourth column in Figure 2. The fourth column shows the MAP-AEM estimates using the same incorrect forward matrix $A(\mu_{a,*}, \mu'_{s,*})$.

A notable feature in the reconstructions is that estimate of h has lower contrast in the reconstructions with the approximation error model than in the reconstructions with the conventional noise model. This can be explained by the fact that covariance of the combined noise $e + \varepsilon$ is larger than the covariance of random noise (i.e.,

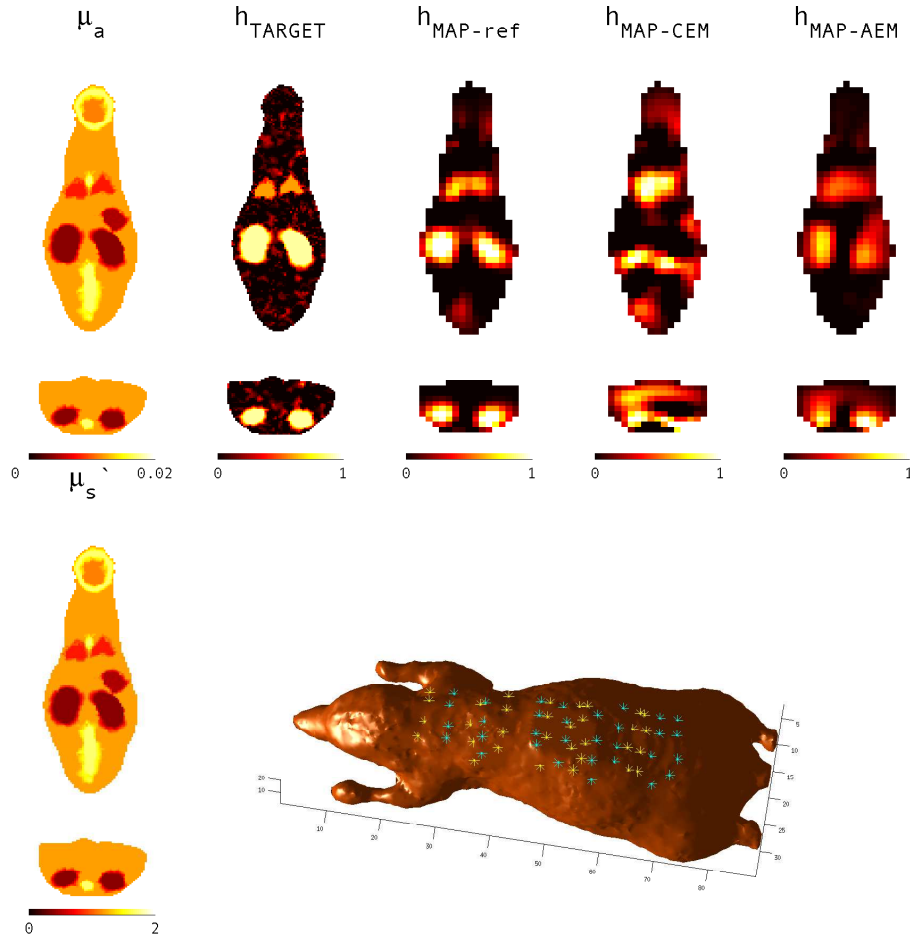


FIGURE 4. First column: target μ_a (top) and μ'_s (bottom) at one horizontal and vertical slices of 3D mouse model. The second column shows the respective slices target fluorophore distribution h of the body. Third column shows MAP-ref estimate using the correct absorption and scattering values (forward matrix $A(\mu_a, \mu'_s)$). Fourth column shows MAP-CEM estimate using the incorrect absorption and scattering values (forward matrix $A(\mu_{a,*}, \mu'_{s,*})$). Fifth column shows MAP-AEM estimates using the same incorrect forward matrix $A(\mu_{a,*}, \mu'_{s,*})$. Bottom-right: Mouse surface with position of sources marked with yellow asterisk(*) and position of detectors marked with blue asterisks.

$\Gamma_e + \Gamma_\varepsilon > \Gamma_e$), implying that the relative weight of the data residual term compared to the prior (or regularization) term becomes smaller in the MAP estimate with the approximation error model compared to the conventional noise model. Thus, the estimate gets, loosely speaking, drawn more strongly towards the prior mean, leading to a loss of contrast. This is also seen from the error estimates in Table 1. In the first row which corresponds to the case that $(\mu_{a,*}, \mu'_{s,*})$ are correct, the

estimation error with the approximation error model is larger than with the conventional noise, and this discrepancy in the error arises from the lower contrast in the estimate of h with the approximation error model. However, when the values $(\mu_{a,*}, \mu'_{s,*})$ are incorrect, rows 2-5 in Table 1 and Figure 3, the estimation error with the approximation error model is smaller than with the conventional noise model, and moreover, the estimation error does not change much as the distance of $(\mu_{a,*}, \mu'_{s,*})$ from the true values (μ_a, μ'_s) increases when moving from row 2 to row 5 in the Table and Figure.

In Figure 4 we show simulation using a realistic 3D mouse model where we simulated high accumulation of fluorophores in the kidneys and lungs of the mouse. To make the simulation physiologically realistic we simulated background physiology by adding random fluorophore concentration $h = \max(h', 0)$ where $h' \sim \mathcal{N}(0, \sigma^2 \mathbb{I})$ with $\sigma = 0.2 \text{mm}^{-1}$, all over the mouse domain except the lungs and kidneys. The localisation of fluorophores in the kidney and lung positions can be seen in the MAP-ref estimates (column 3 Figure 4). They appear slightly distorted in the MAP-CEM estimates (column 4 Figure 4). However, the fluorophore concentrations are relatively better localised in the MAP-AEM estimate (column 5 Figure 4) with a slight loss of contrast.

6. Conclusions. In this paper the recovery from errors caused by incorrectly modeled absorption and scattering in fDOT was considered. Born ratio is known to tolerate artefacts due to unknown absorption and scattering to some extent. However, in case the absorption and scattering properties are highly heterogeneous, incorrectly modelled absorption and scattering induces errors in the fDOT reconstructions.

In this paper, the Bayesian approximation error approach was applied for the compensation of the errors caused by unknown absorption and scattering in fDOT. The modeling errors caused by the inaccurately known absorption and scattering were modeled as an additive modeling error noise in the observation model, and the posterior density model was then marginalized approximately over the unknown modeling errors by using a Gaussian approximation for the joint statistics of the primary unknown (fluorophore concentration) and the modeling errors.

The approach was tested with 2D simulations with various target distributions of absorption and scattering. The results show that the approximation error model can efficiently compensate for the reconstruction artefacts caused by unknown absorption and scattering coefficients, even in the cases of highly heterogeneous absorption and scattering coefficients where the conventional estimates using the Born ratio contained severe artefacts. The approach was also tested with a 3D simulation using a mouse atlas. The MAP estimates using the Bayesian approximation error model show better localisation of the fluorophore concentration compared to the conventional estimate with the normalised Born approximation model.

A tradeoff of the Bayesian approximation error model was found to be a small loss in contrast of the estimated fluorophore concentrations. We suggest that the approximation error model would be a feasible complement to the Born ratio model for handling the uncertainty related to the unknown absorption and scattering parameters in fDOT.

Acknowledgements. The work was supported by the Academy of Finland (projects 119270, 136220, 140984, 272803, and 250215 Finnish Centre of Excellence in Inverse Problems Research 2006-2011). The work was also supported by LASERLAB-EUROPE (grant agreement no. 284464, EC's Seventh Framework Programme).

REFERENCES

- [1] A. Corlu, R. Choe, T. Durduran, M. A. Rosen, M. Schweiger, S. Arridge, M. D. Schnall, and A. G. Yodh, “Three-dimensional in vivo fluorescence diffuse optical tomography of breast cancer in humans,” *Opt. Exp.* **15**(11), 6696–671 (2007).
- [2] V. Ntziachristos, J. Ripoll, L. V. Wang, and R. Weissleder, “Looking and listening to light: the evolution of whole-body photonic imaging,” *Nat. Biotech.* **23**(3), 313 – 320 (2005).
- [3] E. E. Graves, J. Ripoll, R. Weissleder, and V. Ntziachristos, “A submillimeter resolution fluorescence molecular imaging system for small animal imaging,” *Med. Phys.* **30**(5), 901–911 (2003).
- [4] R. Schulz, J. Ripoll, and V. Ntziachristos, “Experimental fluorescence tomography of tissues with noncontact measurements,” *IEEE Trans. Med. Imag.* **23**, 492–500 (2004).
- [5] V. Ntziachristos, C. H. Tung, C. Bremer, and R. Weissleder, “Fluorescence molecular tomography resolves protease activity in vivo,” *Nat. Med.* **8**(7), 757 – 761 (2002).
- [6] S. C. Davis, K. S. Samkoe, J. A. O’Hara, S. L. Gibbs-Strauss, H. L. Payne, P. J. Hoopes, K. D. Paulsen, and B. W. Pogue, “MRI-coupled fluorescence tomography quantifies EGFR activity in brain tumors,” *Acad. Radiol.* **17**(3), 271 – 276 (2010).
- [7] S. Patwardhan, S. Bloch, S. Achilefu, and J. Culver, “Time-dependent whole-body fluorescence tomography of probe bio-distributions in mice,” *Opt. Express* **13**, 2564–2577 (2005).
- [8] H. Shih and V. Ntziachristos, “In vivo characterization of Her-2/neu carcinogenesis in mice using fluorescence molecular tomography,” *Proc. Biomed. Opt.*, OSA (2006).
- [9] A. Koenig, L. Herv, V. Jossierand, M. Berger, J. Boutet, A. Da Silva, J. M. Dinten, P. Pelti, J. L. Coll, and P. Rizo, “In vivo mice lung tumor follow-up with fluorescence diffuse optical tomography,” *J. Biomed. Opt.* **13**(1), 011008 (2008).
- [10] A. Martin, J. Aguirre, A. Sarasa-Renedo, D. Tsoukatou, A. Garofalakis, H. Meyer, C. Marmalaki, J. Ripoll, and A. M. Planas, “Imaging changes in lymphoid organs in vivo after brain ischemia with three-dimensional fluorescence molecular tomography in transgenic mice expressing green fluorescent protein in T lymphocytes,” *Mol. Imag.* **7**(4) (2008).
- [11] M. Solomon, B. R. White, R. E. Nothdruff, W. Akers, G. Sudlow, A. T. Eggebrecht, S. Achilefu, and J. P. Culver, “Video-rate fluorescence diffuse optical tomography for in vivo sentinel lymph node imaging,” *Biomed. Opt. Express* **2**, 3267–3277 (2011).
- [12] V. Ntziachristos, E. A. Schellenberger, J. Ripoll, D. Yessayan, E. Graves, A. Bogdanov, L. Josephson, and R. Weissleder, “Visualization of antitumor treatment by means of fluorescence molecular tomography with an annexin VCy5.5 conjugate,” *Proc. Natl. Acad. Sci. U.S.A.* **101**(33), 12294–12299 (2004).
- [13] J. P. Culver, R. Choe, M. J. Holboke, L. Zubkov, T. Durduran, A. Slep, V. Ntziachristos, D. N. Pattanayak, B. Chance, and A. G. Yodh, “Three-dimensional diffuse optical tomography in the parallel plane transmission geometry: evaluation of a hybrid frequency domain/continuous wave clinical system for breast imaging,” *Med. Phys.* **30**, 235247 (2003).
- [14] S. V. D. Ven, A. Wiethoff, T. Nielsen, B. Brendel, M. V. D. Voort, R. Nachabe, M. Mark, M. Beek, L. Bakker, L. Fels, S. Elias, P. Luijten, and W. Mali, “A novel fluorescent imaging agent for diffuse optical tomography of the breast: First clinical experience in patients,” *Mol. Imag. Biol.* **12**(3), 343–348 (2010).
- [15] S. J. Erickson, S. L. Martinez, J. DeCerce, A. Romero, L. Caldera, and A. Godavarty, “Three-dimensional fluorescence tomography of human breast tissues in vivo using a hand-held optical imager,” *Phys. Med. Biol.* **58**(5), 1563 (2013).
- [16] V. Ntziachristos, A. Hielscher, A. Yodh, and B. Chance, “Diffuse optical tomography of highly heterogeneous media,” *IEEE Trans. Med. Imag.* **20**, 470–478 (2001).
- [17] T. J. Rudge, V. Y. Soloviev, and S. R. Arridge, “Fast image reconstruction in fluorescence optical tomography using data compression,” *Opt. Lett.* **5**, 763–765 (2010).
- [18] J. Kaipio and E. Somersalo, *Statistical and Computational Inverse Problems.*, Springer, New York (2005).
- [19] J. Kaipio and E. Somersalo, “Statistical inverse problems: discretization, model reduction and inverse crimes,” *J. Comput. Appl. Math.* **198** (2007).
- [20] A. Nissinen, L. Heikkinen, and J. Kaipio, “Approximation errors in electrical impedance tomography - an experimental study,” *Meas. Sci. Technol.* **19** (2008).
- [21] A. Lehtikainen, S. Finsterle, A. Voutilainen, L. M. Heikkinen, M. Vauhkonen, and J. P. Kaipio, “Approximation errors and truncation of computational domains with application to geophysical tomography,” *Inv. Probl. Imag.* **1**, 371–389 (2007).

- [22] S. Pursiainen, "Two-stage reconstruction of a circular anomaly in electrical impedance tomography," *Inv. Probl.* **22**(5), 1689 (2006).
- [23] A. Nissinen, L. M. Heikkinen, V. Kolehmainen, and J. P. Kaipio, "Compensation of errors due to discretization, domain truncation and unknown contact impedances in electrical impedance tomography," *Meas. Sci. Technol.* **20**, 105504 (2009).
- [24] S. R. Arridge, J. P. Kaipio, V. Kolehmainen, M. Schweiger, E. Somersalo, T. Tarvainen, and M. Vauhkonen, "Approximation errors and model reduction with an application in optical diffusion tomography," *Inv. Probl.* **22**, 175–195 (2006).
- [25] V. Kolehmainen, M. Schweiger, I. Nissilä, T. Tarvainen, S. R. Arridge, and J. P. Kaipio, "Approximation errors and model reduction in three-dimensional diffuse optical tomography," *J. Opt. Soc. Am. A.* **26**(10), 2257–2268 (2009).
- [26] J. Heino and E. Somersalo, "A modelling error approach for the estimation of optical absorption in the presence of anisotropies," *Phys. Med. Biol.* **49**, 4785–4798 (2004).
- [27] J. Heino, E. Somersalo, and J. Kaipio, "Compensation for geometric mismodelling by anisotropies in optical tomography," *Opt. Express* **13**, 296–308 (2005).
- [28] D. Calvetti, J. P. Kaipio, and E. Somersalo, "Aristotelian prior boundary conditions," *Int. J. Math.* **1**, 63–81 (2006).
- [29] T. Tarvainen, V. Kolehmainen, A. Pulkkinen, M. Vauhkonen, M. Schweiger, S. R. Arridge, and J. P. Kaipio, "An approximation error approach for compensating for modelling errors between the radiative transfer equation and the diffusion approximation in diffuse optical tomography," *Inv. Probl.* **26**, 015005 (2010).
- [30] V. Kolehmainen, T. Tarvainen, S. R. Arridge, and J. P. Kaipio, "Marginalization of uninteresting distributed parameters in inverse problems - application to diffuse optical tomography," *Int. J. Uncertainty Quantification* **1**(1), 1–17 (2011).
- [31] M. Mozumder, T. Tarvainen, S. R. Arridge, J. Kaipio, and V. Kolehmainen, "Compensation of optode sensitivity and position errors in diffuse optical tomography using the approximation error approach," *Biomed. Opt. Express* **4**, 2015–2031 (2013).
- [32] M. Mozumder, T. Tarvainen, J. P. Kaipio, S. R. Arridge, and V. Kolehmainen, "Compensation of modeling errors due to unknown domain boundary in diffuse optical tomography," *J. Opt. Soc. Am. A* **31**, 1847–1855 (2014).
- [33] J. Huttunen and J. Kaipio, "Approximation errors in nonstationary inverse problems," *Inv. Probl. Imag.* **1**(1), 77–93 (2007).
- [34] J. Huttunen and J. Kaipio, "Approximation error analysis in nonlinear state estimation with an application to state-space identification," *Inv. Probl.* **23**, 2141–2157 (2007).
- [35] A. Seppanen, A. Voutilainen, and J. P. Kaipio, "State estimation in process tomography - reconstruction of velocity fields using eit," *Inv. Probl.* **25**(8), 085009 (2009).
- [36] B. Dogdas, D. Stout, A. Chatziioannou, and R. M. Leahy, "Digimouse: A 3D Whole Body Mouse Atlas from CT and Cryosection Data," *Phys. Med. Biol.* **52**, 577–87 (2007).
- [37] Q. Fang, "Digimouse atlas FEM mesh," URL: <http://mcx.sourceforge.net/cgi-bin/index.cgi?MMC/DigimouseMesh>.
- [38] D. Calvetti and E. Somersalo, *An Introduction to Bayesian Scientific Computing Ten Lectures on Subjective Computing*, Springer (2007).
- [39] J. Kaipio and V. Kolehmainen, "Approximate marginalization over modelling errors and uncertainties in inverse problems," in *Bayesian Theory and Applications*, P. Damien, P. Dellaportas, N. G. Polson, and D. A. Stephens, Eds., 644–672, Oxford university press (2013).
- [40] Y. Tan and H. Jiang, "Diffuse optical tomography guided quantitative fluorescence molecular tomography," *Appl. Opt.* **47**, 2011–2016 (2008).
- [41] V. Y. Soloviev, C. D'Andrea, G. Valentini, R. Cubeddu, and S. R. Arridge, "Combined reconstruction of fluorescent and optical parameters using time-resolved data," *Appl. Opt.* **48**, 28–36 (2009).
- [42] Y. Lin, H. Yan, O. Nalcioglu, and G. Gulsen, "Quantitative fluorescence tomography with functional and structural a priori information," *Appl. Opt.* **48**, 1328–1336 (2009).
- [43] T. Correia, N. Ducros, C. D'Andrea, M. Schweiger, and S. Arridge, "Quantitative fluorescence diffuse optical tomography in the presence of heterogeneities," *Opt. Lett.* **38**, 1903–1905 (2013).
- [44] A. Ishimaru, *Wave Propagation and Scattering in Random Media*, Academic, Newyork (1978).
- [45] H. Rue and L. Held, *Gaussian Markov Random Fields: Theory and Applications*, vol. 104 of *Monographs on Statistics and Applied Probability*, Chapman & Hall, London (2005).

- [46] V. Kolehmainen, A. Vanne, S. Siltanen, S. Jarvenpaa, J. Kaipio, M. Lassas, and M. Kalke, "Parallelized bayesian inversion for three-dimensional dental x-ray imaging," *IEEE Trans. Med. Imag.* **25**, 218–228 (2006).
- [47] C. Lieberman, K. Willcox, and O. Ghattas, "Parameter and state model reduction for large-scale statistical inverse problems," *SIAM J. Sci. Comput.* **32**, 2523–2542 (2010).
- [48] M. Schweiger, S. R. Arridge, and I. Nissilä, "Gauss-Newton method for image reconstruction in diffuse optical tomography," *Phys. Med. Biol.* **50**, 2365–2386 (2005).

Received xxxx 20xx; revised xxxx 20xx.

E-mail address: meghdoot.mozumder@uef.fi

E-mail address: tanja.tarvainen@uef.fi

E-mail address: jari@math.auckland.ac.nz

E-mail address: cosimo.dandrea@polimi.it

E-mail address: ville.kolehmainen@uef.fi